PERGAMON

Engineering Fracture Mechanics 67 (2000) 229–249

Engineering Fracture Mechanics

www.elsevier.com/locate/engfracmech

Mixed-mode, high-cycle fatigue-crack growth thresholds in Ti–6Al–4V
II. Quantification of crack-tip shielding

J.P. Campbell, R.O. Ritchie *

Department of Materials Science and Mineral Engineering, University of California, 463 Evans Hall, Berkeley, CA 94720, USA

Received 27 December 1999; received in revised form 4 May 2000; accepted 11 May 2000

Abstract

The role of crack-tip shielding in influencing mixed-mode (mode I + II) fatigue-crack growth thresholds for large, through-thickness cracks in a Ti–6Al–4V turbine blade alloy is examined under high-cycle fatigue loading conditions, i.e., at a loading frequency of 1000 Hz in ambient temperature air for load ratios (K_{min}/K_{max}) of $R = 0.1$–0.8. Techniques are developed to quantify crack-tip shielding with respect to both the mode I and mode II applied loading, enabling an estimation of the shielding-corrected, crack-driving forces actually experienced at the crack tip ($\Delta K_{I,TH,eff}$ and $\Delta K_{II,TH,eff}$ or $\Delta G_{TH,eff}$). In Part I, it was shown that when the crack-driving force is characterized in terms of the range in strain-energy release rate, ΔG, which incorporates contributions from both the applied tensile and shear loading, the mixed-mode (I + II) fatigue-crack growth resistance increases monotonically with the ratio $\Delta K_{II}/\Delta K_I$. When the fatigue-crack growth thresholds are expressed in terms of the near-tip (shielding-corrected) crack-driving force, this increase in crack-growth resistance with increasing mode mixity is markedly reduced. Moreover, for all mode mixities investigated, the near-tip mixed-mode fatigue threshold is lower than the applied (global) value, with the effect being particularly pronounced under shear-dominant loading conditions. These observations illustrate the prominent role of crack-tip shielding for the mixed-mode loading of fatigue cracks with crack-wake dimensions large compared with microstructural size scales; specifically, they indicate that the elevation of the ΔG_{TH} fatigue-crack growth threshold with increasing applied mode mixity is largely due to a shear-induced enhancement of crack-tip shielding.

Keywords: High-cycle fatigue; Fatigue thresholds; Mixed mode; Crack-tip shielding

1. Introduction

The unexpected failure of turbine engine components due to high-cycle fatigue (HCF) loading conditions [1,2] currently represents one of the primary threats to the safety and readiness of US military aircraft fleets. The occurrence of such failures is extremely costly; moreover, attempts to control the problem substantially

* Corresponding author. Tel.: +510-486-5798; fax: +510-486-4995.
E-mail address: roritchie@lbl.gov (R.O. Ritchie).

0013-7944/00/$ - see front matter
PII: S0013-7944(00)00047-3

increase the cost associated with this phenomenon, both in terms of equipment "down-time" and expenses associated with component inspection. Multiaxial loading conditions are known to exist at some fatigue-critical locations within turbine engine components, particularly in association with fretting fatigue in the blade dovetail/disk contact section [3]. In the presence of cyclic multiaxial loading, the resultant crack-driving force may be a combination of the influence of a mode I (tensile opening) stress-intensity range, ΔK_I, as well as mode II (in-plane shear) and/or mode III (anti-plane shear) stress-intensity ranges, ΔK_{II} and ΔK_{III}, respectively. Whereas most published fatigue thresholds are reported for (nominally) pure mode I loading, several studies have demonstrated that superimposed cyclic shear (ΔK_{II} or $\Delta K_{III} > 0$) can lower the value of ΔK_I at threshold [4–12], sometimes markedly [13].

Since the high loading frequencies (~1–2 kHz) and correspondingly short failure times associated with HCF may necessitate a threshold-based design methodology [14], it is important that the effect of mode mixity (i.e., the applied ratio of shear to tensile loading) on fatigue-crack growth resistance is characterized for aircraft engine materials. For the Ti–6Al–4V blade alloy of interest here, it has been shown in Part I of this paper [15] that the presence of mixed-mode cyclic loading conditions does not preclude the application of such a threshold-based design criterion. Indeed, the threshold fatigue-crack growth resistance is observed to increase monotonically with the applied ratio of ΔK_{II} to ΔK_I, such that the pure mode I threshold (expressed in terms of the range in strain energy release rate, ΔG) may be used as a conservative estimate of the mixed-mode (I + II) fatigue-crack growth threshold for $\Delta K_{II}/\Delta K_I > 0$.

In the present work, mixed-mode, fatigue-crack growth thresholds for combined mode I + II loading are investigated for a Ti–6Al–4V alloy in the bimodal (STOA) microstructural condition (a typical turbine engine blade microstructure). The influence of various combinations of shear and tensile loading, ranging from $\Delta K_{II}/\Delta K_I = 0$ (mode I loading) to ~7 on the crack-growth threshold condition is reported for loading conditions characteristic of turbine engine HCF, i.e., high mean stresses (up to $R = 0.8$) and high cyclic loading frequencies (1000 Hz). The mechanistic origins of the measured increase in the fatigue-crack growth threshold, ΔG_{TH}, with increasing applied phase angle, β ($= \tan^{-1}(\Delta K_{II}/\Delta K_I)$), described in Part I [15], are investigated through the development of sample-compliance-based techniques to quantify crack-tip shielding with respect to the applied mode I and mode II crack-driving forces, ΔK_{II} and ΔK_{II}, respectively. Such shielding is considered to occur by crack wedging (i.e., crack closure) in mode I and additionally by sliding crack-surface interference when mode II is superimposed. More specifically, when fatigue fracture surfaces are sheared with respect to one another, the transmission of the applied shear loading to the crack tip can be mitigated both by the development of frictional stress in the crack wake and by the interlocking of fracture surface asperities. Using the compliance-based techniques, quantitative estimates are made of the shielding-corrected crack-driving forces actually experienced at the crack tip ($\Delta K_{I,TH,eff}$ and $\Delta K_{II,TH,eff}$ or $\Delta G_{TH,eff}$). When the fatigue thresholds are expressed in terms of the near-tip (shielding-corrected) driving force, threshold values are decreased and the increase in crack-growth resistance with increasing mode mixity is markedly reduced. This implies that the elevation of the mixed-mode, large-crack threshold (in terms of ΔG_{TH}) with increasing mode mixity can be attributed primarily to a shear-induced enhancement in crack-tip shielding.

2. Experimental procedures

2.1. Material

The material investigated was a forged Ti–6Al–4V turbine engine alloy received in a bimodal microstructural condition (nearly equiaxed primary α with lamellar $\alpha + \beta$ colonies). Full details of the composition, processing, heat treatment, section sizes and microstructural features are given in Part I of this paper

[15]. In the longitudinal orientation, the material displays mean yield and tensile strengths of 930 and 978 MPa, respectively [16].

2.2. Experimental methods

As described in Part I of this paper [15], mixed-mode thresholds for fatigue cracks, large compared to microstructural dimensions, were measured using the asymmetric four point bend (AFPB) specimen [4,17–19]. Mixed-mode loading conditions (applied to a mode I fatigue pre-crack) were quantified both in terms of the ratio $\Delta K_{II}/\Delta K_I$, which was varied from 0 (pure mode I) to 7.1, and the phase angle, β ($= \tan^{-1}(\Delta K_{II}/\Delta K_I)$), which correspondingly varied from 0° to 82°. Positive load ratios ($R = K_{min}/K_{max}$) were varied between 0.1 and 0.8. Fatigue testing was performed at 1000 Hz (sine wave) on a MTS servo-hydraulic, high-frequency testing machine incorporating a voice-coil servovalve [20]. Procedures for determining the fatigue thresholds, and for the prior pre-cracking of the AFPB samples, can also be found in Part I [15].

The extent of crack-tip shielding caused by crack-surface contact was evaluated using in situ measurements of the mode I and mode II compliance curves of the test sample (i.e., applied load as a function of mode I and mode II crack-opening displacement) during cyclic loading at the fatigue-crack growth threshold condition. Compliance curves were recorded using a crack-opening displacement (COD) gauge mounted on the side surface of the sample, approximately 1 mm behind the crack tip. For measurement of the mode I compliance, the COD gauge was bonded directly to the side of the sample, as indicated in Fig. 1a. Measurement of the mode II compliance curve required that the fixture shown in Fig. 1b be placed between the sample and the COD gauge. Compliance curves were recorded at a cyclic loading frequency of 1 Hz and applied values of ΔK_I and ΔK_{II} corresponding to the fatigue-crack growth threshold for the load ratio and phase angle, β, of interest. Such measurements were made following the application of 1 million

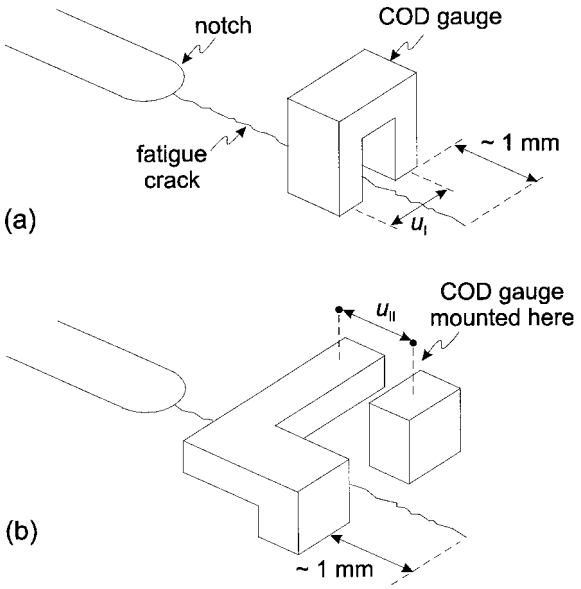

Fig. 1. Compliance curves were recorded using a COD gauge mounted on the side surface of the sample approximately 1 mm behind the crack tip. For measurement of the mode I compliance, (a) the COD gauge was bonded directly to the side of the sample. Measurement of the mode II compliance curve required that a fixture (b) be placed between the sample and the COD gauge. The COD gauge shown in (a) was then bonded to the surface of this fixture, at the location indicated in (b).

cycles at 1000 Hz cyclic loading frequency and this same loading amplitude. This pre-measurement cycling was intended to allow any cycle-dependent degradation of crack-wake contact due to fracture surface wear and abrasion to occur and (presumably) to reach steady state.

The mode I closure stress intensity, K_{cl}, was estimated using the known pre-crack length and the load, P_{cl}, corresponding to the onset of fracture surface contact (i.e., wedging) during unloading. P_{cl} was taken at the first deviation from linearity in the mode I unloading compliance curve [21,22]. The effective, threshold, mode I, stress-intensity range experienced at the crack tip was then defined as

$$\Delta K_{I,TH,eff} = K_{I,max} - K_{cl}, \tag{1}$$

where $K_{I,max}$ is the maximum applied value of the mode I stress intensity.

The technique, which was developed for estimating the magnitude of shielding with respect to the applied value of ΔK_{II}, is considered to be a significant result of the present work. For this reason, a detailed description of this technique will be deferred to the results and discussion section of this paper. As will be shown, it was possible to infer the maximum and minimum (local) values of K_{II} actually experienced at the crack tip, $K^{tip}_{II,max}$ and, $K^{tip}_{II,min}$ respectively, using the mode II loading and unloading compliance curves. The effective, threshold, mode II, stress-intensity range experienced at the crack tip was then defined according to the following relationship:

$$\Delta K_{II,TH,eff} = K^{tip}_{II,max} - K^{tip}_{II,min}. \tag{2}$$

Using the techniques described above, the measured mixed-mode, fatigue-crack growth thresholds were compared in terms of both the applied crack-driving force and the near-tip, shielding-corrected driving force.

3. Results and discussion

3.1. Mixed-mode fatigue-crack growth thresholds

The mixed-mode fatigue-crack growth thresholds for bimodal Ti–6Al–4V, in terms of the mode II stress-intensity range at threshold, $\Delta K_{II,TH}$, as a function of the corresponding mode I threshold, $\Delta K_{II,TH}$, are shown in Fig. 2 for mode mixities of $\Delta K_{II}/\Delta K_I = 0$, 0.5, 1.9 and 7.1 ($\beta = 0°$, 26°, 62° and 82°, respectively) and load ratios of 0.1, 0.5 and 0.8. Closed and open symbols represent the loading conditions that produced, respectively, no crack growth and crack growth; these loading conditions bound the true threshold for the onset of crack extension. While these data are in general agreement with mixed-mode fatigue-crack growth behavior reported in other material systems [4,8–11,23,24], as noted in Part I [15], an interesting feature is present which has not been previously reported for mixed-mode fatigue thresholds. Specifically, the value of mode I threshold, $\Delta K_{I,TH}$, is slightly increased as β is increased from 0° to 26°, which gives rise to the appearance of a "nose" in the threshold envelope. As discussed below, this insensitivity of $\Delta K_{I,TH}$ to superimposed shear loading at phase angles below ~60° can be attributed largely to a shear-induced enhancement of the mode I fatigue-crack closure. Over the wider range of mode mixities though, the mode I $\Delta K_{I,TH}$ threshold decreases with increasing β. However, as noted in Part I, when threshold data are plotted in terms of the range in strain energy release rate, ΔG, or the equivalent stress intensity, ΔK_{eq} (Fig. 3), viz,

$$\Delta G_{TH} = (\Delta K^2_{I,TH} + \Delta K^2_{II,TH})/E' = \Delta K^2_{eq,TH}/E', \tag{3}$$

the pure mode I threshold ($\beta = 0°$), in terms of ΔG_{TH} or $\Delta K_{eq,TH}$, is the worst case [15]. In Eq. (3), $E' = E/(1 - \nu^2)$ in plane strain and E in plane stress, where E is Young's modulus and ν is Poisson's ratio.

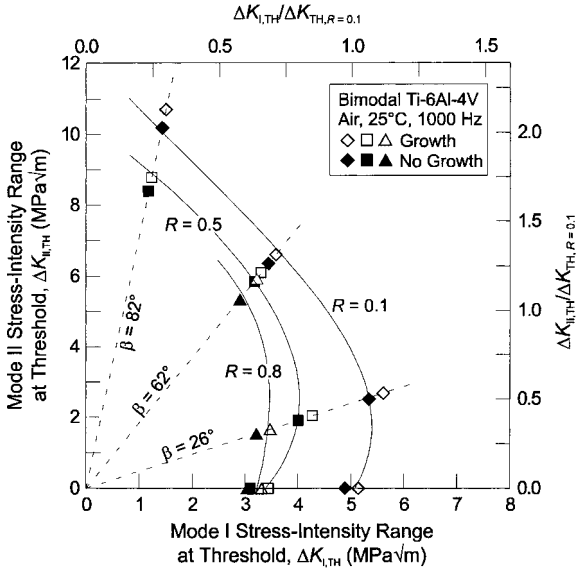

Fig. 2. Mixed-mode, fatigue-crack growth threshold envelopes for bimodal Ti–6Al–4V at load ratios, R, of 0.1, 0.5 and 0.8 and a cyclic loading frequency of 1000 Hz in ambient temperature air. Closed and open symbols represent the loading conditions that produced, respectively, no crack growth and crack growth; these loading conditions bound the true threshold for the onset of crack extension. On the upper and right-hand axes, $\Delta K_{I,TH}$ and $\Delta K_{II,TH}$ are normalized by the pure mode I threshold at $R = 0.1$, $\Delta K_{TH,R=0.1}$.

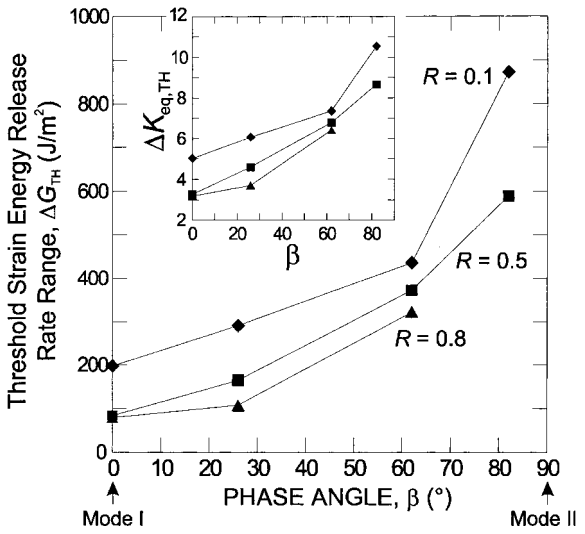

Fig. 3. Mixed-mode, fatigue-crack growth thresholds in bimodal Ti–6Al–4V are plotted in terms of the range in strain energy release rate at threshold, ΔG_{TH}, as a function of the applied phase angle, $\beta(= \tan^{-1}(\Delta K_{II}/\Delta K_I))$, for load ratios of 0.1, 0.5 and 0.8. ΔG_{TH} is observed to increase substantially with β. Inset: the equivalent stress-intensity range, $\Delta K_{eq,TH}(= (\Delta G_{TH} E')^{1/2})$, is plotted as a function of β.

3.2. Mixed-mode crack-tip shielding

The important role of wake interference in mixed-mode fatigue-crack growth has been well documented in the literature. There have been numerous experimental observations about the effects of crack-wake interference [4,11,24–28] and attempts to model this fracture surface interaction and the associated crack-tip shielding [25,29–31]. However, there does not yet exist a simple experimental technique for quantifying crack-tip shielding with respect to an applied mode II loading, akin to the well developed techniques for quantifying such crack-wake effects during pure mode I fatigue. For mode I loading, crack closure is routinely quantified using a rather simple in situ unloading compliance curve measurement on the fatigue test sample [22]. Using the same compliance curve, it also possible to quantify [32,33] any crack bridging [34–36] which might be present. In the following paragraphs, simple experimental techniques (based upon the measurement of sample compliance curves) for quantifying crack-tip shielding with respect to both mode I and mode II loading in the presence of superimposed shear and tensile loading are described. Using these techniques, the magnitude of crack-tip shielding is measured for bimodal Ti–6Al–4V, and these shielding measurements are used to present the mixed-mode fatigue-crack growth threshold data shown in Figs. 2 and 3 in terms of the crack-driving force actually experienced at the crack tip.

Fatigue-sample compliance curves (loading and unloading) were determined for both mode I and mode II displacements, using the near-tip COD gauge described above. The general form of these curves is shown schematically in Fig. 4. Note that the mode I compliance curve measured during mixed-mode loading (Fig. 4a) is essentially identical to that measured for pure mode I fatigue. The form of the mode II compliance curve shown in Fig. 4b (actual experimental data are shown in Fig. 4c) is a generalization which captures all of the essential features observed for such curves at different values of β and R; these features are discussed below.

At this point, it should be noted that the measured compliance curves for a subordinate loading mode [1] were not interpretable in the manner which will be described in the following sections. In other words, the features of the compliance curves which are used here to aid in quantification of crack-tip shielding were not discernable in these compliance curves. Thus, measurements of crack-tip shielding with respect to the applied mode II loading were only made for shear-dominant loading conditions ($\Delta K_{II}/\Delta K_I > 1$), and mode I crack-tip shielding was quantified only for tensile dominant conditions ($\Delta K_{II}/\Delta K_I < 1$). The distortion of the subordinate mode compliance curves is attributed to the large displacement imposed on the COD gauge (by the dominant loading mode) in a direction orthogonal to that in which the gauge is designed to make measurements. Such effects could be magnified by any misalignment of the gauge.

3.2.1. Mode I crack-tip shielding

Mode I crack-tip shielding, i.e., crack closure, was quantified for tensile-dominant mixed-mode loading ($\Delta K_{II}/\Delta K_I = 0.5$, $\beta = 26°$) and pure mode I loading ($\Delta K_{II}/\Delta K_I = 0$, $\beta = 0°$) using the well established technique of defining the closure load, P_{cl}, as the load corresponding to the first deviation from linearity in the mode I unloading compliance curve. The mode I closure stress intensity, K_{cl}, was then calculated using P_{cl}, the known crack length, and a mode I stress-intensity solution for bending [37]. Measured values of K_{cl} are presented in Fig. 5 in terms of $K_{cl}/K_{I,max}$ (where $K_{I,max}$ is the maximum mode I stress intensity) as a function of R for $\beta = 0°$ and 26°. Note that the absolute values of K_{cl} are indicated adjacent to the data points.

[1] The term "subordinate loading mode" is most easily defined by the use of the following examples. For $\Delta K_{II}/\Delta K_I = 0.5$ ($\beta = 26°$), the shear loading mode is subordinate while the tensile loading mode is dominant, i.e., $\Delta K_I > \Delta K_{II}$. Conversely, for $\Delta K_{II}/\Delta K_I = 1.9$ and 7.1 ($\beta = 62°$ and 82°, respectively), the shear loading mode is dominant and the tensile mode is subordinate.

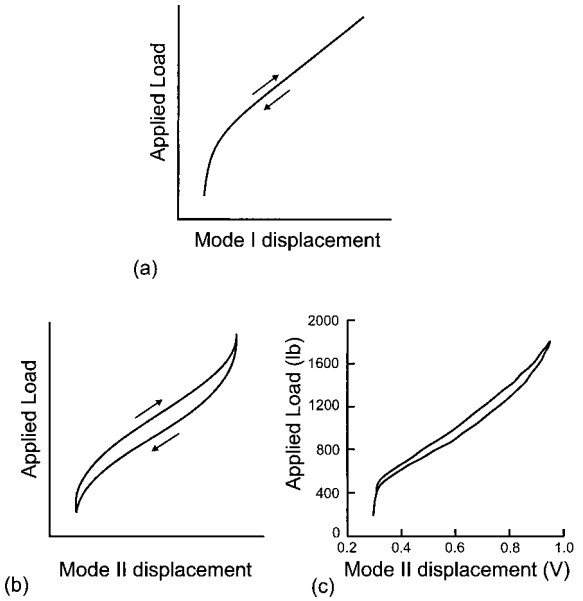

Fig. 4. Representation of the general form observed for, (a) mode I and (b) mode II compliance curves measured using a side-mounted, near-tip COD gauge. Actual experimental data for the mode II compliance behavior are shown in (c).

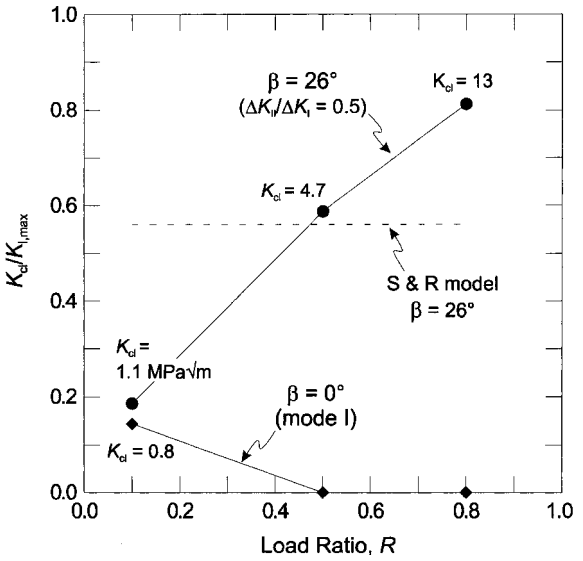

Fig. 5. Measured values of the mode I closure stress intensity, K_{cl}, (normalized by the maximum mode I stress intensity, $K_{I,max}$) are presented as a function of load ratio, R, for $\beta = 0°$ and 26°. Note that values of K_{cl} (not normalized by $K_{I,max}$) are indicated adjacent to the data points. While fatigue crack closure is observed to be suppressed by increasing load ratio for mode I loading ($\beta = 0°$), K_{cl} increases rather dramatically with load ratio when a small amount of shear loading is superimposed ($\beta = 26°$, $\Delta K_{II}/\Delta K_I = 0.5$). Experimental results are compared with a prediction based upon the model of Suresh and Ritchie ("S and R" model [41]).

In Fig. 5, it is apparent that, for mode I loading ($\beta = 0°$), crack closure is suppressed as load ratio increases. In fact, closure appears to be completely eliminated at $R = 0.5$ and 0.8. It should be noted that these values of K_{cl} for $\beta = 0°$ are somewhat lower than previous reports of mode I crack closure in this same

material [38]. This small disparity may be due to differences in the technique employed to measure the unloading compliance curve (side-mounted, near-tip COD gauge in the current study; back-face-strain compliance in Ref. [38]).

In stark contrast to the behavior exhibited for $\beta = 0°$, the mode I closure stress intensity for $\beta = 26°$ ($\Delta K_{II}/\Delta K_I = 0.5$) is observed to increase markedly as load ratio increases from 0.1 to 0.8. Measured values of K_{cl} are 1.1, 4.7 and 13.0 MPa $\sqrt{m}$, respectively, at $R = 0.1$, 0.5 and 0.8; corresponding values of $K_{cl}/K_{I,max}$ are 0.19, 0.59 and 0.81. While the assertion that crack closure is operative at $R = 0.8$ may be surprising, supporting fractographic evidence can be seen in Fig. 6, which shows scanning electron photomicrographs of the fatigue surfaces in the near-tip crack wake for $R = 0.1$ and 0.8 at $\beta = 26°$. In both images, evidence of fracture surface contact is present in the form of "wear scars" produced by the relative shear displacements of the fracture surfaces. These wear scars are characterized by flat regions with parallel surface markings oriented exactly in the direction of the relative shear displacement between the fracture surfaces during cyclic loading. At $R = 0.1$, these markings tend to be larger in size, occupy more area on the fracture surface, and have more wear debris surrounding them than at $R = 0.8$. This suggests more extensive

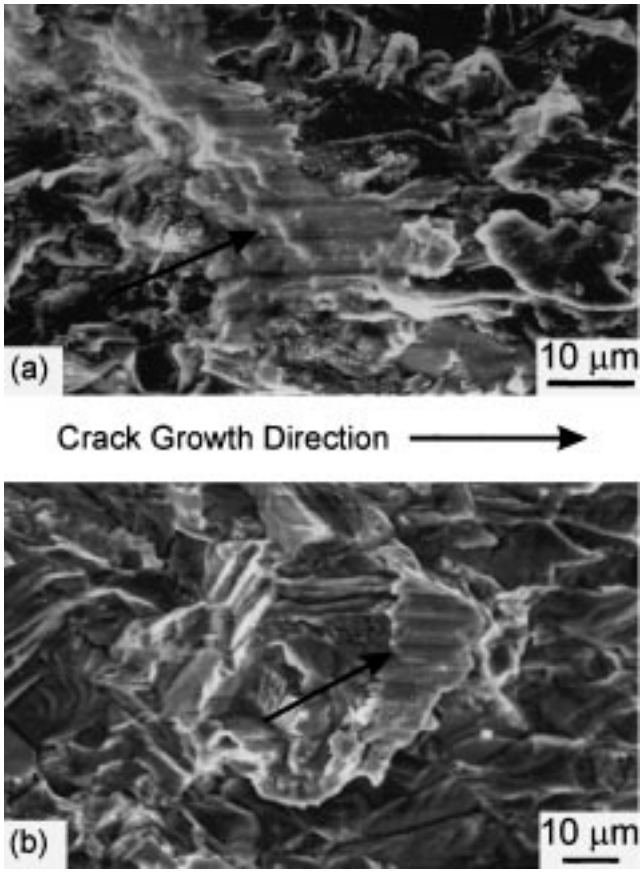

Fig. 6. Scanning electron photomicrographs of the fatigue fracture surfaces in the near-tip crack wake are shown for (a) $R = 0.1$ and (b) $R = 0.8$ at $\beta = 26°$. In both images, evidence of fracture surface contact is present in the form of "wear scars" (indicated by arrows) produced by the relative shear displacements of the fracture surfaces; these wear scars are characterized by flat regions with parallel surface markings oriented exactly in the direction of the relative shear displacement (left to right) between the fracture surfaces during cyclic loading. At $R = 0.1$, considerable debris is observed around the wear scar.

fracture surface contact for $R = 0.1$; nonetheless, the presence of these features at $R = 0.8$ indicates that fracture surface contact does occur at this high value of load ratio.

The dramatic increase in K_{cl} with increasing load ratio for $\beta = 26°$ is believed to result from a shear-induced offsetting of the fracture surface asperities. While it is known that some amount of mode II crack opening generally occurs even for nominally mode I loading [39], clearly the amount of mode II displacement in the crack wake is increased when $\beta > 0°$. An increase in the level of crack closure under mixed-mode loading conditions has previously been reported in a 2024-T3 aluminum alloy [40]. Such shear-induced enhancement of mode I closure has been modeled by Suresh and Ritchie [41]. Using a very simple idealization of a rough fatigue fracture surface, with asperities of high h and width W, and a geometrical consideration of crack surface contact, they derive an expression for K_{cl} as

$$K_{cl}/K_{I,max} = \{2\gamma x/(1 + 2\gamma x)\}^{1/2}, \tag{4}$$

where $x = u_{II}/u_I$ is the ratio of mode II to mode I displacements in the crack wake and $\gamma = h/W$, the ratio of fracture surface asperity height to width. Characterization of the fatigue pre-crack fracture surfaces in the present study indicates that $\gamma = 0.46$. Using this value of γ and assuming that $u_{II}/u_I = \Delta K_{II}/\Delta K_I = 0.5$ for $\beta = 26°$, Eq. (4) predicts $K_{cl}/K_{I,max} = 0.56$. In contrast to the experimental data, this predicted value of $K_{cl}/K_{I,max}$ is independent of load ratio (Fig. 5), a contradiction that is believed to be an artifact of the perfectly periodic fracture surface modeled by Suresh and Ritchie. In reality, fracture surfaces are not so regular, and it is likely that the maximum height differential of fracture surface asperities which may come into contact during mode I unloading will increase as the magnitude of shear offset of the fracture surfaces increases. This would explain the observed increase in $K_{cl}/K_{I,max}$ with load ratio. For the measured fatigue-crack growth thresholds at $\beta = 26°$, the mean value of K_{II} increases from ~1.6 to 7.2 MPa $\sqrt{m}$ as R increases from 0.1 to 0.8. In addition, the assumption that $u_{II}/u_I = \Delta K_{II}/\Delta K_I$ is questionable, as it is known that this relationship does not necessarily hold for mode I loading, where it has been shown that $u_{II}/u_I \neq 0$ even though $\Delta K_{II}/\Delta K_I = 0$ [39]; moreover, models of shear-induced fracture surface contact indicate that this contact can cause the near-tip mode mixity to differ markedly from the applied value of $\Delta K_{II}/\Delta K_I$ [31].

Using the measured values of K_{cl}, an effective, near-tip, mode I, stress-intensity range at threshold, $\Delta K_{I,TH,eff}$, can be defined according to Eq. (1). $\Delta K_{I,TH,eff}$ represents the mode I crack-driving force actually experienced at the crack tip after the effects of crack closure have been "subtracted" from the far-field, applied driving force. When K_{cl} is less than the minimum applied value of K_I, closure is not active and $\Delta K_{I,TH,eff}$ is equal to the applied value of $\Delta K_{I,TH}$.

Consideration in this manner of the influence of fatigue-crack closure on the near-tip mode I crack-driving force provides an explanation for the "nose" which is observed in the mixed-mode fatigue-crack growth threshold envelopes (Fig. 2). Recall that this nose is a manifestation of the fact that the mode I stress-intensity range at threshold, $\Delta K_{I,TH}$, does not decrease monotonically as the magnitude of shear loading (and hence phase angle, β) increases. Instead, the value of $\Delta K_{I,TH}$ increases slightly (for $R = 0.1$ and 0.5) or remains constant ($R = 0.8$) as β increases from 0° to 26° (Fig. 7). However, when the mode I crack-driving forces are considered in terms of the "closure-corrected" near-tip values, $\Delta K_{I,TH,eff}$, the increase in the mode I threshold stress-intensity range as β increases from 0° to 26° is no longer observed (or at least is significantly reduced). This is illustrated in Fig. 7, where $\Delta K_{I,TH,eff}$ and $\Delta K_{I,TH}$ are compared as a function of the applied phase angle, β. While it is important to remember that the measured values of K_{cl} represent only an approximate quantification of crack-tip shielding, these data strongly suggest that the nose which is observed in the mixed-mode fatigue-crack growth threshold envelope is largely a result of a shear-induced enhancement of mode I crack closure.

The measured variation of K_{cl} with R for $\beta = 26°$ also provides some insight regarding the relationship between ΔG_{TH} and R (Fig. 8), which was previously discussed in Part I of this paper. The transition between a region of relatively strong load ratio dependence (for $R < 0.5$) and relatively weak load ratio dependence

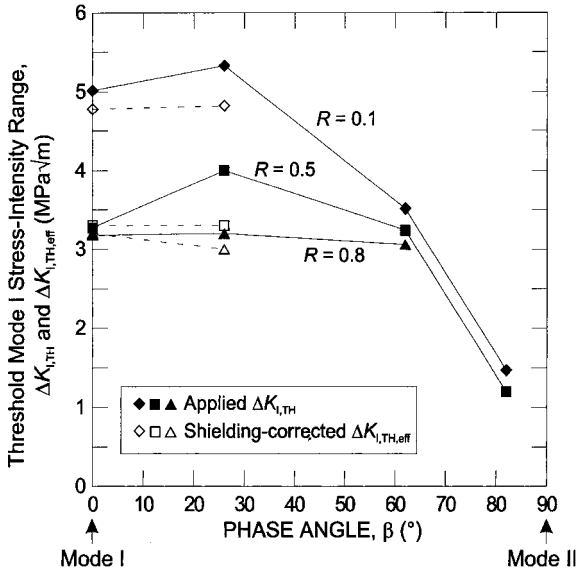

Fig. 7. The mode I stress-intensity range at threshold is plotted as a function of applied phase angle, β, both in terms of the applied $\Delta K_{I,TH}$ and the near-tip, shielding-corrected $\Delta K_{I,TH,eff}$. The slight increase in $\Delta K_{I,TH}$, which is observed when β increases from 0° (mode I loading) to 26° ($\Delta K_{II}/\Delta K_I = 0.5$) is essentially eliminated when the effects of crack closure are "subtracted" from the near-tip, crack-driving force, which is characterized by $\Delta K_{I,TH,eff}$.

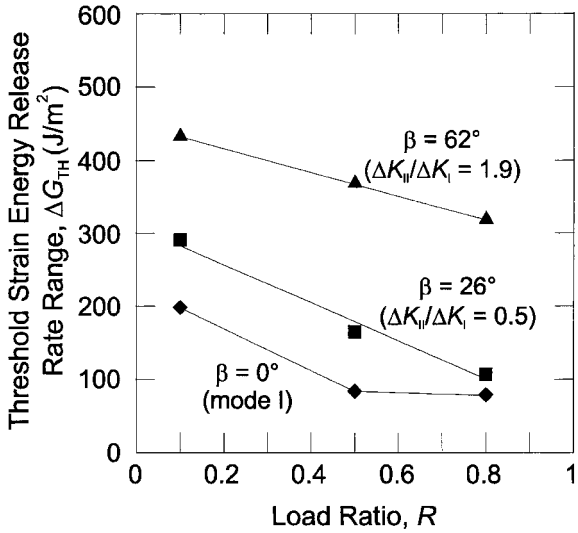

Fig. 8. The threshold range in strain energy release rate, ΔG_{TH}, is plotted as a function of load ratio, R, for $\beta = 0°$, 26° and 62° ($\Delta K_{II}/\Delta K_I = 0$, 0.5 and 1.9, respectively). For each value of β, the fatigue-crack growth threshold decreases as load ratio increases.

(for $R > 0.5$), which is exhibited by the pure mode I threshold data ($\beta = 0°$) arises primarily from a suppression of crack closure at higher load ratios [42]. The lack of such a transition for threshold data measured at $\beta = 26°$ appears to result from the fact that crack closure persists for load ratios up to $R = 0.8$.

Moreover, it is speculated that the absence of a transition between regimes of strong and weak load ratio dependence for the shear-dominant threshold data ($\beta = 62°$) is also due to the fact that crack-wake contact mechanisms are operative over the entire range of load ratio investigated. As quantified below, crack-wake contact mechanisms are found to be operative for all load ratios investigated at $\beta = 62°$ and 82°.

3.2.2. Mode II crack-tip shielding

Shielding with respect to the applied mode II loading is believed to arise due to both the development of frictional resistance to a relative shear displacement of the fatigue fracture surfaces, which inhibits but does not preclude relative motion, and mechanical interlock of fracture surface asperities, where any (local) relative motion of the fracture surfaces is severely restricted and must be accompanied by elastic or plastic deformation of the interlocking asperities. Such mode II shielding was quantified for all load ratios at $\beta = 62°$ and 82° ($\Delta K_{II}/\Delta K_I = 1.9$ and 7.1), with the exception of the loading condition $R = 0.8$ and $\beta = 82°$, for which the fatigue-crack growth threshold has not been measured. To measure the magnitude of the effective, near-tip mode II crack-driving force at threshold, $\Delta K_{II,TH,eff}$, the following technique, which requires measurement of both the loading and unloading compliance curves, was developed. These compliance curves were determined using a COD gauge mounted approximately 1 mm behind the crack tip (Fig. 1).

The COD gauge employed consisted of a "c-section" of aluminum with strain gauges mounted on both cantilever arms. Likewise, the fixture for measuring mode II crack-wake displacements was machined from aluminum. Both the COD gauge and mode II fixture were adhesively bonded to the measurement surface; the area of contact (both above and below the crack) between the gauge and sample and between the mode II fixture and sample were approximately 1.5 mm (in the direction of displacement measurement) by 4 mm. Prior to attachment, both the COD gauge and mode II fixture were situated using a micrometer-equipped alignment and positioning fixture; this ensured precise placement of the gauge with respect to the crack tip and proper alignment with respect to the desired direction of measurement (mode I or mode II displacements).

An idealization of the general form of the resulting mode II compliance curve (applied load as a function of mode II crack-wake displacement) is shown in Fig. 9a. With respect to quantification of crack-tip shielding, the relevant features of this curve are best illustrated by considering it to be a composite of the following curves. In the absence of any crack-wake contact mechanisms, one would expect the mode II compliance curve to be perfectly linear, as shown in Fig. 9b. However, for a fatigue crack in a polycrystalline material, the crack path is generally somewhat tortuous, such that the fatigue fracture surfaces will come into contact with one another during mixed-mode loading. This fracture surface contact can be manifested as a frictional resistance to the shear displacement of the fracture surfaces with respect to one another. Frictional resistance to mode II crack-wake displacements will give rise to a mode II compliance curve characterized by hysteresis, as shown in Fig. 9c. The "knees" which are observed for the initial portions of both the loading and unloading curves (indicated as points a and b in Fig. 9c) are an indication of frictional locking of the crack wake following a reversal in loading direction. The form of this curve has previously been theorized by Smith and Smith [25].

In addition to developing frictional resistance to mode II shearing of the fracture surfaces, crack-wake contact can also result in asperity interlock, where asperities come into contact and, due to mechanical interlock, are prevented from displacing relative to one another. When such interlock occurs, the contacting asperities will deform elastically or plastically under the influence of the applied shear loading, and may eventually fracture. In Fig. 10, a scanning electron photomicrograph shows the crack-wake profile (imaged at the sample surface) resulting from a fatigue-crack growth threshold measurement at $R = 0.5$ and $\beta = 82°$. Interlocking asperities (indicated by arrows) show evidence of extensive deformation due to the applied shear loading.

The occurrence of asperity interlock will tend to increase the apparent stiffness of the sample as the locked portions of the crack wake will behave like uncracked ligaments. The experimentally observed mode

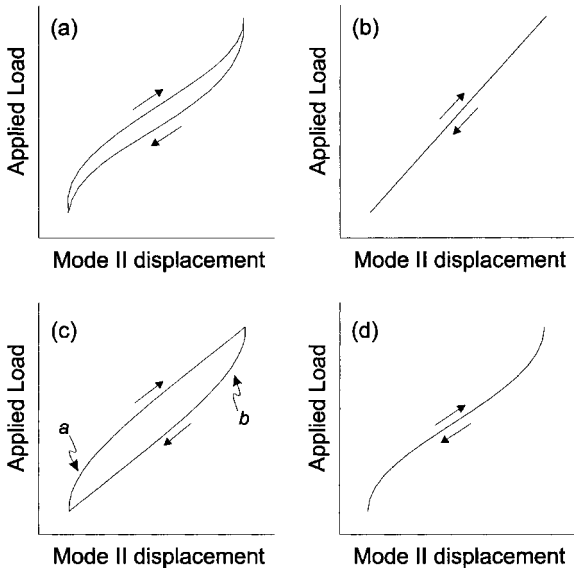

Fig. 9. The disparity between the general form of the mode II compliance curve, shown in (a), and the single linear loading and unloading curve (b), which would be exhibited in the absence of any crack-wake contact mechanisms, can be attributed to the presence of friction and asperity interlock in the fatigue-crack wake during the application of mixed-mode loading. For frictional resistance only to the relative shear displacements in the crack wake, the mode II compliance curve would appear as shown in (c). Here, the "knees" in the loading and unloading curves (indicated as points a and b, respectively) are a result of frictional locking in the crack wake following a reversal in loading direction. With significant asperity interlock present at the extremes of the applied loading cycle (but not friction), the compliance curve will appear as in (d). The observed loading and unloading mode II compliance curve (a) can be viewed as a composite of the curves shown in (b)–(d).

II compliance curves suggest that appreciable asperity interlock is most likely to develop near the maximum and minimum applied load, where the fracture surface asperities are, respectively, most out of registry or being prevented (by contact mechanisms) from returning to registry (Fig. 11). Asperity interlock in the crack wake, in the absence of friction, [2] will produce a compliance curve of the form shown in Fig. 9d. The features of the experimentally measured compliance curve (Fig. 9a) should now be recognizable as the traction-free, linear elastic curve (Fig. 9b), modified by the presence of crack-wake friction and asperity interlock.

Using this rationalization, the effective, near-tip, mode II, crack driving force at threshold, $\Delta K_{\mathrm{II,TH,eff}}$, can now be estimated by the construction illustrated in Fig. 12. The following assumptions are made: (i) the mode II crack-tip opening displacement ($\mathrm{CTOD_{II}}$), measured very near to the crack tip (such that appreciable shielding cannot develop between the point of measurement and the actual crack tip), is characteristic of the actual value of K_{II} experienced at the crack tip, (ii) the maximum and minimum displacements, measured by the near-tip COD gauge, correspond to the points in the loading cycle where the $\mathrm{CTOD_{II}}$ is, respectively, a maximum and minimum, and (iii) the single, straight-line compliance curve which sample loading and unloading would follow in the absence of friction and asperity interlock (the wake-contact-free compliance) can be approximated as the average of the linear portions of the measured

[2] The condition of interlock in the absence of friction is not likely to occur in a real crack wake, as the asperity contact which gives rise to interlock (a near complete suppression of relative motion of the crack faces) is an extreme case of that which produces friction (inhibition of relative motion). However, consideration of this condition aids in the interpretation of the form of the mode II compliance curve without compromising the validity of the theory being presented here.

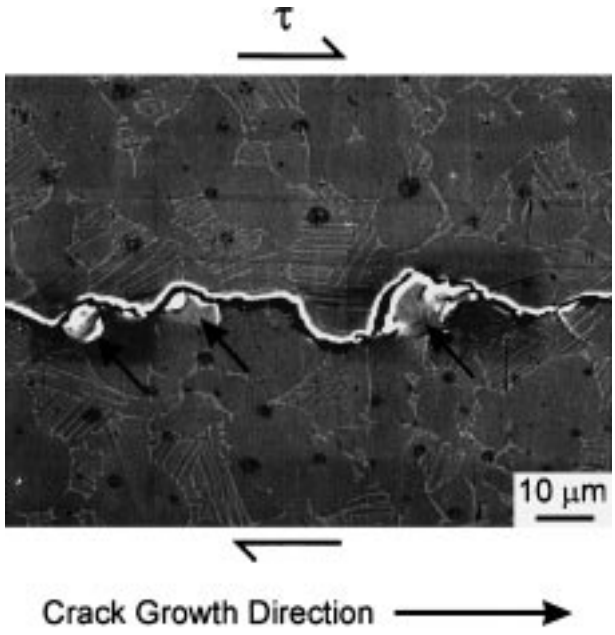

Fig. 10. A scanning electron photomicrograph shows the crack-wake profile (recorded at the sample surface) resulting from a fatigue-crack growth threshold measurement at $R = 0.5$ and $\beta = 82°$. Interlocking asperities (indicated by arrows) show evidence of extensive deformation due to impingement under the applied shear loading.

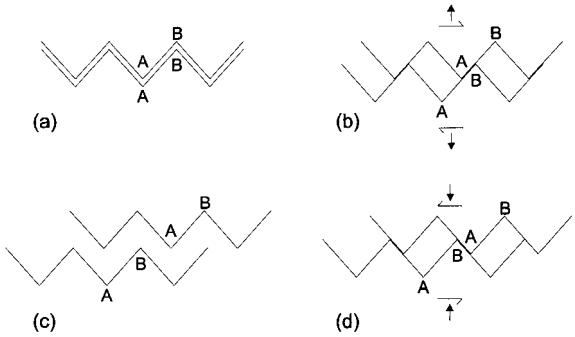

Fig. 11. This schematic illustration provides insight into the mechanistic origin of asperity interlock at the minimum of the applied cyclic loading waveform. In (a), mating fracture surface asperities are shown prior to the first application of mixed-mode loading. In (b), asperity contact is observed during the first loading cycle, as the fracture surfaces are both opened and sheared with respect to one another. At the maximum of the loading cycle (c), the asperities are observed to be out of registry. In (d), it is shown how, upon unloading, the asperities may come into contact in a manner which does not allow the mating fracture surfaces to regain registry at the minimum of the loading cycle, thus giving rise to asperity interlock.

loading and unloading compliance curve (Fig. 12); these linear portions of the measured compliance curves are observed to occur near the mean load.

As shown in Fig. 12, the loads corresponding to the maximum and minimum values of K_{II} experienced at the crack tip are then determined by the intersections of the maximum and minimum mode II crack-wake displacements, $u_{II,max}$ and $u_{II,min}$, with the wake-contact-free compliance curve (points a and b). From the

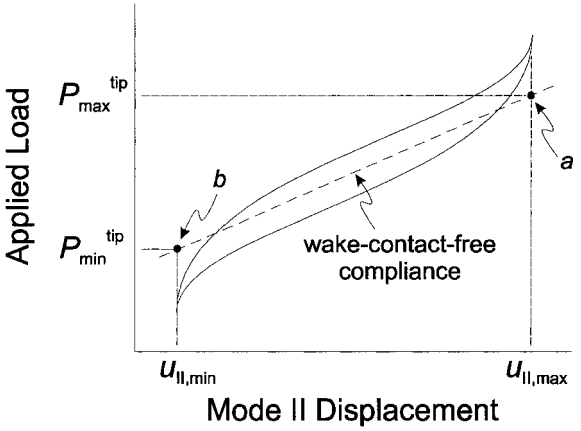

Fig. 12. The effective, near-tip, mode II, crack-driving force at threshold, $\Delta K_{II,TH,eff}$, can be estimated by finding the loads, P_{max}^{tip} and P_{min}^{tip}, at which the maximum and minimum mode II crack opening displacements intersect the wake-contact-free compliance curve. P_{max}^{tip} and P_{min}^{tip} can then be used in conjunction with the known crack length to calculate $K_{II,max}^{tip}$ and $K_{II,min}^{tip}$. The near-tip, mode II, crack-driving force is then estimated as $\Delta K_{II,TH,eff} = K_{II,max}^{tip} - K_{II,min}^{tip}$.

second assumption above, these maximum and minimum displacements are representative of the $CTOD_{II}$ extrema. The points a and b on the wake-contact-free compliance curve indicate the applied loads, P_{max}^{tip} and P_{min}^{tip}, which would be necessary to produce these $CTOD_{II}$ extrema in the absence of any crack-wake shielding mechanisms. Thus, P_{max}^{tip} and P_{min}^{tip} can be used with the known crack length and the mode II stress-intensity solution for asymmetric four point bending [18] to calculate the maximum and minimum values of the mode II stress intensity experienced at the crack tip, $K_{II,max}^{tip}$ and $K_{II,min}^{tip}$. An effective, near-tip, threshold, mode II stress-intensity range (from which the effects of crack-tip shielding have been removed) can then be calculated as

$$\Delta K_{II,TH,eff} = K_{II,max}^{tip} - K_{II,min}^{tip}.$$

Table 1 presents a comparison of the applied and effective, near-tip values of the mode II stress-intensity ranges at threshold; also shown is magnitude of the shielding, expressed as the reduction in $\Delta K_{II}(= \Delta K_{II,TH} - \Delta K_{II,TH,eff})$.

The data presented in Table 1 illustrate that a significant portion of the applied mode II driving force can be absorbed by crack-tip shielding; for example, for $R = 0.1$ and $\beta = 82°$, only 46% of the applied mode II stress-intensity range is transmitted to the crack tip. Inspection of the data indicates that for both $\beta = 62°$ and 82°, the reduction in ΔK_{II} due to crack-tip shielding decreases with increasing load ratio. This trend is consistent with physical intuition; as load ratio increases (for a fixed value of β), the fatigue crack is more open during the entirety of the loading cycle (due to the elevated magnitudes of K_I) and shear-induced,

Table 1
Comparison of applied and shielding-corrected, near-tip, mode II stress-intensity ranges

Load ratio, R	Phase angle, β (°)	$\Delta K_{II,TH}$ (MPa $\sqrt{m}$)	$\Delta K_{II,TH,eff}$ (MPa $\sqrt{m}$)	Reduction in ΔK_{II} (MPa $\sqrt{m}$)[a]
0.1	62	6.5	3.9	2.6
	82	10.4	4.8	5.6
0.5	62	6.0	4.6	1.4
	82	8.6	5.3	3.3
0.8	62	5.6	5	0.6

[a] The reduction in ΔK_{II} is equal to $\Delta K_{II,TH} - \Delta K_{II,TH,eff}$.

crack-wake contact will be reduced. Also, consistent with physical intuition is the observation that for both $R = 0.1$ and 0.5, the reduction in ΔK_{II} due to crack-tip shielding increases with mode mixity. An increase in phase angle, β, is accompanied by an increase in the magnitude of the applied shear loading and a decrease in the magnitude of tensile opening of the crack; under these conditions, crack-wake contact would be expected to increase.

3.3. Shielding-corrected mixed-mode thresholds

Using the measurements of mode I and mode II crack-tip shielding and the associated definitions of the near-tip mode I and mode II crack-driving forces (Eqs. (1) and (2)), it is now possible to rationalize the measured fatigue threshold data (Figs. 2 and 3) in terms of the driving force actually experienced at the crack tip. Although the meaning of mode I "crack closure" is somewhat altered for shear-dominant loading conditions, where the fatigue fracture surfaces are seemingly in contact during the entirety of the loading cycle (as evidenced by the occurrence of asperity interlock and frictional resistance to mode II crack-wake displacements), the notion of a reduction in the applied ΔK_I by a wedging open of the crack continues to apply. As discussed below, consideration of the shielding-corrected fatigue thresholds gives considerable insight into the mechanism for the increase in fatigue-crack growth resistance with increasing mode mixity, observed in Fig. 3.

In Fig. 13, the mixed-mode fatigue-crack growth threshold envelopes for $R = 0.1$, 0.5 and 0.8 are presented in terms of both the applied and near-tip (shielding-corrected) values of ΔK_I and ΔK_{II}. For the sake of simplicity, each threshold is presented simply as a single data point which is the average of the measured growth/no growth conditions given in Fig. 2. Applied values of the mode I and mode II driving forces ($\Delta K_{I,TH}$ and $\Delta K_{II,TH}$) are plotted as filled symbols with a solid line envelope; corresponding values of the

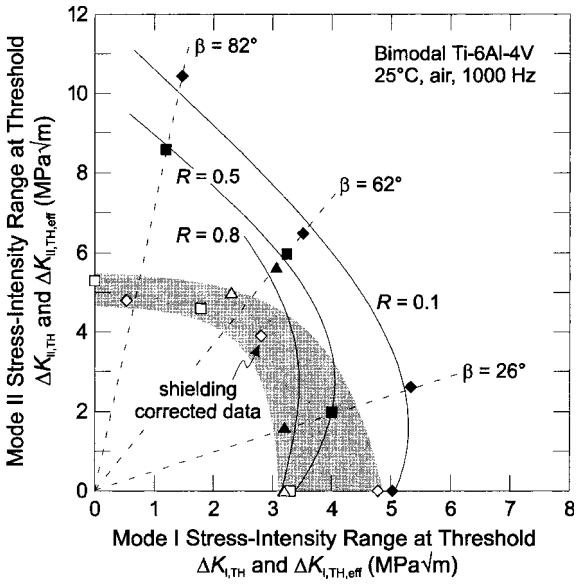

Fig. 13. Mixed-mode, fatigue-crack growth threshold envelopes for $R = 0.1$, 0.5 and 0.8 are presented in terms of both the applied threshold stress-intensity ranges, $\Delta K_{I,TH}$ and $\Delta K_{II,TH}$ (▲, ◆, ■) and the near-tip, shielding-corrected values, $\Delta K_{I,TH,eff}$ and $\Delta K_{II,TH,eff}$ (△, ◇, □). For shear-dominant loading conditions, the shielding-correct fatigue thresholds are considerably lower than those based upon the applied values of crack-driving force.

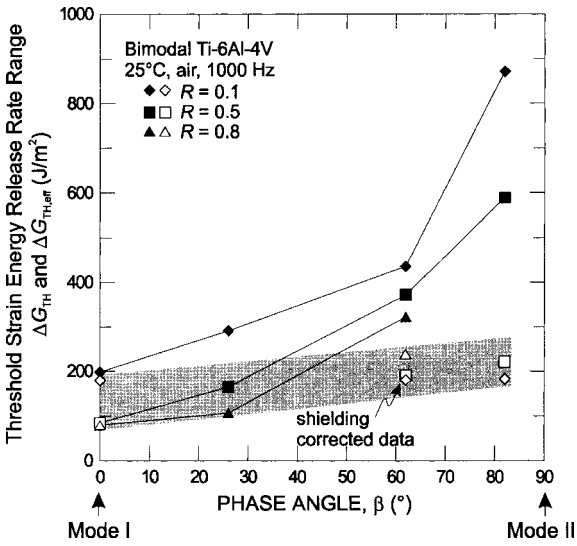

Fig. 14. Mixed-mode, fatigue-crack growth thresholds at $R = 0.1$, 0.5 and 0.8 are presented in terms of both the applied value of ΔG_{TH} (represented by ▲, ◆, ■) and the shielding-corrected, near-tip driving force, $\Delta G_{TH,eff}$ (△, ◇, □) as a function of the applied phase angle, β. From these data, it is apparent that the dramatic rise in fatigue-crack growth resistance (characterized by ΔG_{TH}) with increasing β is largely due to the development of extensive crack-tip shielding.

near-tip (shielding-corrected) driving forces ($\Delta K_{I,TH,eff}$ and $\Delta K_{II,TH,eff}$) are given by open data symbols bounded by a single scatter band. [3] It is apparent that the fatigue thresholds measured for shear-dominant loading conditions (applied β of 62° and 82°) are well scaled at all load ratios by plotting the data in terms of the near-tip (shielding-corrected), crack-driving forces; indeed, near-tip threshold data for all load ratios fall within a relatively narrow scatter band. [4] Moreover, it is clear that the magnitude of the mixed-mode threshold is significantly reduced in the absence of crack-tip shielding.

For the tensile-dominant loading conditions, e.g. $\beta = 0°$ (pure mode I), the threshold data are not as well scaled by the application of crack-tip shielding corrections. However, this finding is consistent with previous reports of mode I fatigue-crack growth behavior in this same bimodal Ti–6Al–4V [38], where it was noted that the degradation of fatigue-crack growth resistance due to increasing load ratio cannot be explained solely by a consideration of crack closure effects.

In Fig. 14, the mixed-mode fatigue-crack growth thresholds are replotted in terms of the range in strain energy release rate as a function of the applied phase angle. Characterization of the thresholds in terms of the applied value of ΔG_{TH} is represented by closed data point symbols, while the shielding-corrected, near-tip driving force, $\Delta G_{TH,eff} (= \{\Delta K^2_{I,TH,eff} + \Delta K^2_{II,TH,eff}\}/E')$ is represented by open data point symbols. This

[3] Since it was not possible to measure mode I K_{cl} values at $\beta = 62°$ and 82°, as noted above, measured values of K_{cl} at $\beta = 26°$ for the respective load ratios were used as estimates in order to plot $\Delta K_{I,TH,eff}$ in Fig. 13. Because K_{cl} increases with the magnitude of shear offset of the fracture surfaces (Fig. 5), the values of K_{cl} measured at $\beta = 26°$ are believed to be conservative estimates of K_{cl} at $\beta = 62°$ and 82°. As no measurement was made of $\Delta K_{II,TH,eff}$ for $\beta = 26°$, no attempt is made to plot shielding-corrected threshold data for this phase angle.

[4] It is interesting to note here that the ratio of shear to tension ($\Delta K_{II}/\Delta K_I$) experienced at the crack tip is not equal to the applied value of this parameter; this is indicated in Fig. 13 by the fact that the shielding-corrected thresholds do not lie on the lines of constant β, which intersect the non-shielding-corrected data. This alteration of the near-tip phase angle by crack-wake contact has been predicted by theoretical modeling of the fracture surface interactions [31].

plot suggests that mode I loading may continue to be worst case for mixed-mode thresholds characterized in terms of $\Delta G_{TH,eff}$, at least for higher load ratios, e.g., $R = 0.5$ and 0.8. However, while the ΔG_{TH} thresholds are increased by a factor of ~4–7 as β increases from 0° to 82°, in terms of the near-tip (shielding-corrected) $\Delta G_{TH,eff}$ threshold, the increase is at most a factor of ~2.5. In fact, for $R = 0.1$, the $\Delta G_{TH,eff}$ threshold appears to be essentially independent of mode mixity. Moreover, it is apparent that the threshold values for shear-dominant loading conditions are most significantly reduced when crack-tip shielding is "removed" from the applied crack-driving force; the improvement in fatigue-crack growth resistance associated with crack-tip shielding (i.e., the disparity between the shielding-corrected and uncorrected data) is progressively enhanced with increasing mode mixity.

These results provide strong evidence that the enhancement in fatigue-crack growth resistance, observed with increase in $\Delta K_{II}/\Delta K_I$, can be attributed largely to the development of crack-tip shielding due to fracture surface contact mechanisms in the crack wake. However, as noted above, there continues to be a slight increase in crack-growth resistance with increasing applied phase angle, at least for $R = 0.5$ and 0.8 (Fig. 14), even after the effects of shielding have been accounted for (by characterizing in terms of $\Delta G_{TH,eff}$). This suggests that additional mechanisms (aside from crack-tip shielding) may also be operative. It has been shown in Ref. [11] that for equivalent magnitudes of the stress-intensity range (i.e., $\Delta K_{II} = \Delta K_I$), the cyclic plastic-zone size increases by a factor of 3.7 when going from mode I to mode II loading conditions. Moreover, in a related study of interfacial toughness between an elastic–plastic solid and a non-yielding elastic solid, Tvergaard and Hutchinson [43] predict an increasing toughness with increasing applied phase angle due to the development of enhanced crack-tip plasticity in the elastic–plastic material. It is thus possible that the small increase in $\Delta G_{TH,eff}$ with increasing β is a result of such shear-loading enhanced plastic deformation, and hence, increased shear displacements at the crack tip. Clearly, additional work is needed to make any definitive statements in this regard.

It has been shown that in this Ti–6Al–4V alloy, the pure mode I, ΔG_{TH} fatigue-crack growth threshold is lower than that measured for any mixed-mode loading condition. This suggests that for design against HCF, the ΔG_{TH} threshold determined in mode I could be used as a conservative estimate of the mixed-mode, fatigue-crack growth threshold. It is pertinent to note, however, that this conclusion is based on a study of cracks large compared to the scale of the microstructure and which have fracture surface dimensions on the order of several millimeters. The marked decrease in mixed-mode, fatigue-crack growth threshold values, when they are "corrected" for the influence of crack-tip shielding, implies that the mode I ΔG_{TH} threshold may not be as conservative in the presence of small fatigue flaws with limited crack wake. While the results in Fig. 14 and those for short cracks in Part I [15] indicate that, even in the "absence" of crack-tip shielding, the $\Delta G_{TH,eff}$ threshold may still increase somewhat with increasing applied phase angle, it is still not known whether such a shielding-corrected, mode I threshold will remain the lower-bound for cracks that are truly small compared to microstructural dimensions or whether the thresholds for such cracks will fall within the scatter band of $\Delta G_{TH,eff}$ versus β shown in Fig. 14.

3.4. Comparison of short-crack and shielding-corrected, large-crack fatigue thresholds

In Fig. 15, mixed-mode, short-crack, fatigue threshold data for bimodal Ti–6Al–4V are compared with the scatterband of shielding-corrected, large-crack threshold data for $R = 0.1$ to 0.8; further details regarding the short-crack data are given in Part I [15]. The mixed-mode, short-crack threshold data are generally in good agreement with the shielding-corrected, large-crack data, with two of the three measured short-crack thresholds lying within the shielding-corrected scatterband. However, the short-crack fatigue thresholds are at the lower end of, or even slightly below, the shielding-corrected, large-crack data scatterband.

This comparison between the short-crack and shielding-corrected, large-crack threshold data provides some insight regarding the accuracy of the compliance-based techniques developed for quantifying

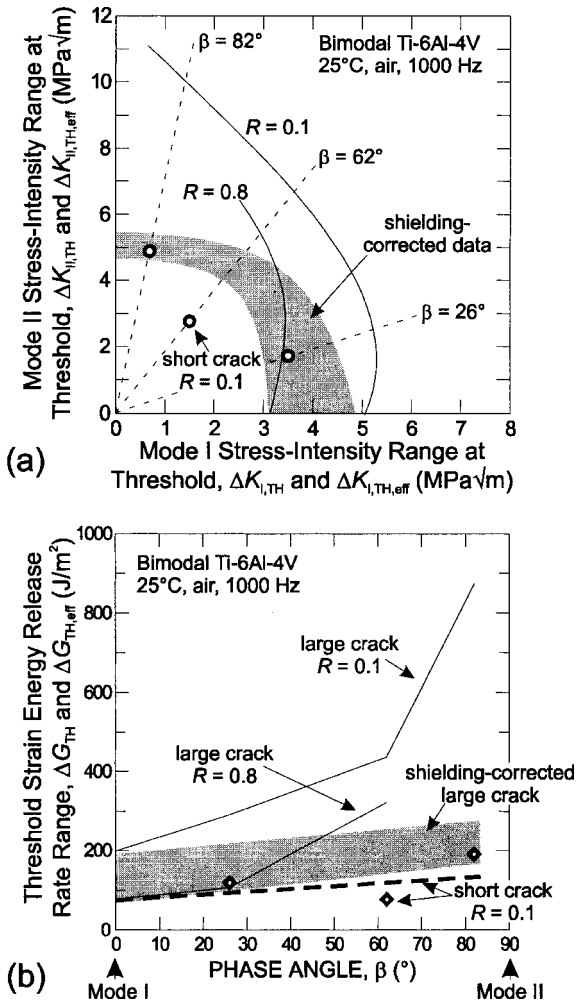

Fig. 15. The short-crack ($R = 0.1$, [15]) and large-crack ($R = 0.1$ and 0.8) mixed-mode, fatigue-crack growth threshold data in bimodal Ti–6Al–4V are compared with a scatterband representing shielding-corrected, large-crack threshold data for $R = 0.1$ to 0.8 both in terms of (a) the mixed-mode threshold envelope and (b) the threshold range in strain energy release rate, ΔG_{TH}, as a function of the applied phase angle, $\beta(= \tan^{-1}(\Delta K_{II}/\Delta K_I))$. The short-crack thresholds are observed to be in reasonably good agreement with the shielding-corrected, large-crack data.

crack-tip shielding during mixed-mode cyclic loading. If it is assumed that the primary difference between the crack-growth behavior of large and short fatigue cracks is the disparity in crack-tip shielding, the observed correspondence of the current short-crack and large-crack, shielding-corrected data suggests that the methods employed to estimate crack-tip shielding are reasonably accurate. However, the fact that the scatterband of the shielding-corrected, large-crack thresholds are shifted to slightly higher fatigue-crack growth resistance compared to the short-crack data suggests that these compliance-based techniques for quantification of mixed-mode shielding may yield slightly non-conservative results. Moreover, it is important to remember that the potential influence of crack-wake-contact mechanisms has not been completely eliminated for the short-fatigue cracks due to the ~200 μm of crack wake which exists (~20 times the average grain size for bimodal Ti–6Al–4V); the magnitude of shielding which can develop within 200

μm of crack wake is unclear. In the complete absence of crack-tip shielding, it is possible that the mixed-mode, fatigue-crack growth thresholds will be somewhat lower than the shielding-corrected, large-crack threshold reported here; in addition, the dependence of the fatigue-crack growth resistance (in terms of ΔG) on the applied phase angle β may well be further reduced.

4. Conclusions

A study has been made of HCF crack-growth thresholds for large (>4 mm) cracks subjected to high frequency (1000 Hz), combined mode I and mode II loading (mode mixities varying from $\Delta K_{II}/\Delta K_I = 0$ to ~7; phase angles from 0° to 82°) in a Ti–6Al–4V turbine blade alloy with a bimodal (STOA) microstructure. Specifically, sample-compliance-based techniques have been employed to quantify the magnitude of the mixed-mode, crack-tip shielding with respect to both the applied mode I and mode II stress-intensity ranges, ΔK_I and ΔK_{II}, respectively, for load ratios ranging from $R = 0.1$ to 0.8. Based on this work, the following conclusions can be made:

(1) The significant increase in the ΔG_{TH} fatigue-crack growth threshold with increasing mode mixity can be attributed primarily to a shear-induced enhancement of crack-tip shielding. As the magnitude of applied shear loading increases, the crack closure stress intensity (which shields the crack tip with respect to the applied mode I loading) increases. Furthermore, extensive shear-induced, crack-wake contact develops, which shields the crack tip with respect to the applied mode II loading. Quantitative estimates of the magnitude of this shear-induced, crack-tip shielding have been made by newly developed, experimental, compliance-based techniques.

(2) The mode I threshold stress-intensity range, $\Delta K_{I,TH}$, is somewhat insensitive to the superposition of shear loading for $\Delta K_{II}/\Delta K_I = 0$ to 1.9 ($\beta = 0°$ to 62°). In fact, for $R = 0.1$ and 0.5, $\Delta K_{I,TH}$ increases slightly as $\Delta K_{II}/\Delta K_I$ increases from 0 to 0.5. This insensitivity of $\Delta K_{I,TH}$ to the increasing magnitude of superimposed shear loading can be attributed primarily to the above mentioned shear-induced enhancement of mode I fatigue-crack closure. For more strongly shear-dominant loading conditions, e.g., $\Delta K_{II}/\Delta K_I = 7.1$ ($\beta = 82°$), the value of $\Delta K_{I,TH}$ is significantly reduced with respect to its value for pure mode I loading.

(3) When the ΔG_{TH} fatigue-crack growth thresholds are characterized in terms of the near-tip (shielding-corrected), crack-driving force, the influence of mode mixity is significantly reduced. Moreover, the influence of load ratio on the fatigue threshold is also reduced for shear-dominant loading conditions (i.e., $\Delta K_{II}/\Delta K_I > 1$), although for tensile-dominant loading conditions, the thresholds continue to be load ratio dependent.

(4) As the ΔG_{TH} fatigue-crack growth threshold for pure mode I is found to be lower than that measured for any other mixed-mode loading condition, this threshold could be considered as a lower-bound estimate of the mixed-mode, fatigue-crack growth threshold under HCF conditions. However, this conclusion has been formulated for cracks of "continuum-size" dimensions; its accuracy in the presence of cracks with microstructural dimensions remains to be tested.

Acknowledgements

This work was supported by the US Air Force Office of Scientific Research under Grant no. F49620-96-1-0478 under the auspices of the Multidisciplinary University Research Initiative on *High Cycle Fatigue* to the University of California.

References

[1] Cowles BA. High cycle fatigue in aircraft gas turbines – an industry perspective. Int J Fract 1996;80:147–63.
[2] Nicholas T, Zuiker JR. On the use of the Goodman diagram for high cycle fatigue design. Int J Fract 1996;80:219–35.
[3] Waterhouse RB, Lindley TC, editors. Fretting Fatigue. European Structural Integrity Society Publication No. 18. Mechanical Engineering Publications, London, 1994.
[4] Gao H, Brown MW, Miller KJ. Mixed-mode fatigue thresholds. Fatig Engng Mater Struct 1982;5:1–17.
[5] Gao H, Alagok N, Brown MW, Miller KJ. Growth of fatigue cracks under combined mode I and mode II loads. In: Miller KJ, Brown MW, editors. Multiaxial fatigue, ASTM STP 853. Philadelphia, PA: ASTM, 1985. p. 184–202.
[6] Pustejovsky MA. Fatigue crack propagation in titanium under general in-plane loading – I: experiments. Engng Fract Mech 1979;11:9–15.
[7] Pustejovsky MA. Fatigue crack propagation in titanium under general in-plane loading – II: analysis. Engng Fract Mech 1979;11:17–31.
[8] Tanaka K. Fatigue crack propagation from a crack inclined to the cyclic tensile axis. Engng Fract Mech 1974;6:493–507.
[9] Tong J, Yates JR, Brown MW. The influence of precracking techniques on fatigue crack growth thresholds under mixed mode I/II loading conditions. Fatigue Fract Engng Mater Struct 1994;17:1261–9.
[10] Tong J, Yates JR, Brown MW. The significance of mean stress on the fatigue crack growth threshold for mixed mode I + II loading. Fatigue Fract Engng Mater Struct 1994;17:829–38.
[11] Zheng YS, Wang ZG, Ai SH. Mixed-mode I and II fatigue threshold and crack closure in dual-phase steels. Metall Mater Trans A 1994;25A:1713–23.
[12] Iida S, Kobayashi AS. Crack-propagation rate in 7075-T6 plates under cyclic tensile and transverse shear loading. J Bas Engng 1969;91:764–9.
[13] John R, DeLuca D, Nicholas T, Porter J. Near-threshold crack growth behavior of a single crystal Ni-base superalloy subjected to mixed mode loading. In: Miller KJ, McDowell DL, editors. Mixed-mode crack behavior, ASTM STP 1359. Philadelphia, PA: ASTM, 1999. p. 312.
[14] Ritchie RO, Davidson DL, Boyce BL, Campbell JP, Roder O. High-cycle fatigue of Ti–6Al–4V. Fatigue Fract Engng Mater Struct 1999;22:621–31.
[15] Campbell JP, Ritchie RO. Mixed-mode, high-cycle fatigue-crack growth thresholds in Ti–6Al–4V. Part I. A comparison of large- and short-crack behavior. Engng Fract Mech 2000;67:209–27.
[16] Eylon D. Summary of the available information on the processing of the Ti–6Al–4V HCF/LCF program plates. University of Dayton Report, 1998.
[17] He MY, Cao HC, Evans AG. Mixed-mode fracture: the four-point shear specimen. Acta Metall Mater 1990;38:839–46.
[18] He MY, Hutchinson JW. Asymmetric four-point crack specimen. J Appl Mech 2000;67:207–9.
[19] Suresh S, Shih CF, Morrone A, O'Dowd NP. Mixed-mode fracture toughness of ceramic materials. J Am Ceram Soc 1990;73:1257–67.
[20] Morgan JM, Milligan WW. A 1 kHz servohydraulic fatigue testing system. In: Soboyejo WO, Srivatsan TS, editors. High Cycle Fatigue of Structural Materials. Philadelphia, PA: TMS, 1997. p. 305–12.
[21] Elber W. Fatigue crack closure under cyclic tension. Engng Fract Mech 1970;2:37–45.
[22] Ritchie RO, Yu W. Short crack effects in fatigue: a consequence of crack tip shielding. In: Ritchie RO, Lankford J, editors. Small Fatigue Cracks. Philadelphia, PA: TMS-AIME, 1986. p. 167–89.
[23] Pook LP. A failure mechanism map for mixed mode I and II fatigue crack growth threshold. Int J Fract 1985;28:R21–3.
[24] Liu P, Wang Z. Mixed-mode I and II fatigue threshold and crack deflection angle in SiCp/2024Al composite. Scripta Mater 1996;34:1323–30.
[25] Smith MC, Smith RA. Toward an understanding of mode II fatigue crack growth. In: Fong JT, Fields RJ, editors. Basic questions in fatigue: vol. I, ASTM STP 924. Philadelphia, PA: ASTM, 1988. p. 260–80.
[26] Tong J, Yates JR, Brown MW. The formation and propagation of mode I branch cracks in mixed mode fatigue failure. Engng Fract Mech 1997;56:213–31.
[27] Nayeb-Hashemi H, McClintock FA, Ritchie RO. Effects of friction and high torque on fatigue crack propagation in mode III. Metall Trans A 1982;13A:2197–204.
[28] Tschegg EK. Sliding mode crack closure and mode III fatigue crack growth in mild steel. Acta Metall 1983;31:1323–30.
[29] Tong J, Yates JR, Brown MW. A model for sliding mode crack closure. I. Theory for pure mode II loading. Engng Fract Mech 1995;52:599–611.
[30] Tong J, Yates JR, Brown MW. A model for sliding mode crack closure. II. Mixed mode I and II loading and application. Engng Fract Mech 1995;52:613–23.
[31] Carlson RL, Beevers CJ. A mixed mode fatigue crack closure model. Engng Fract Mech 1985;22:651–60.
[32] Ritchie RO, Yu W, Bucci RJ. Fatigue crack propagation in ARALL laminates: measurement of the effect of crack-tip shielding from crack bridging. Engng Fract Mech 1989;32:361–77.

[33] Campbell JP, Venkateswara Rao KT, Ritchie RO. The effect of microstructure on fracture toughness and fatigue crack growth behavior in γ-titanium aluminide based intermetallics. Metall Mater Trans A 1999;30A:563–77.
[34] Evans AG. Perspective on the development of high-toughness ceramics. J Am Ceram Soc 1990;73:187–206.
[35] Chan KS. Micromechanics of shear ligament toughening. Metall Trans A 1991;22A:2021–9.
[36] Venkateswara Rao KT, Odette GR, Ritchie RO. Ductile-reinforcement toughening in γ-TiAl intermetallic-matrix composites: effects on fracture toughness and fatigue-crack propagation resistance. Acta Metall Mater 1994;42:893–911.
[37] Tada H, Paris PC, Irwin GR. The Stress Analysis of Cracks Handbook, 2nd ed. St. Louis, MO: Paris Productions, 1985.
[38] Ritchie RO, Boyce BL, Campbell JP, Roder O, Thompson AW, Milligan WW. Thresholds for high-cycle fatigue in a turbine engine Ti–6Al–4V alloy. Int J Fatig 1999;21:653–62.
[39] Davidson DL, Lankford J. Fatigue crack growth in metals and alloys: mechanisms and micromechanics. Int Mater Rev 1992;37:45–76.
[40] Abdel-Mageed AM, Pandey RK. Studies on cyclic crack path and the mixed mode crack closure behavior in Al-alloy. Int J Fatig 1992;14:21–9.
[41] Suresh S, Ritchie RO. A geometric model for fatigue crack closure induced by fracture surface morphology. Metall Trans A 1982;13A:1627–31.
[42] Schmidt RA, Paris PC. Threshold for fatigue crack propagation and effects of load ratio and frequency. In: Progress in flaw growth and fracture toughness testing, ASTM STP 536. Philidelphia, PA: ASTM, 1973. p. 79–94.
[43] Tvergaard V, Hutchinson JW. The influence of plasticity on mixed-mode interface toughness. J Mech Phys Solids 1993;41: 1119–35.